Commun Nonlinear Sci Numer Simulat 78 (2019) 104863

Contents lists available at ScienceDirect

Commun Nonlinear Sci Numer Simulat

journal homepage: www.elsevier.com/locate/cnsns

Research paper

Computational finite element model for surface wrinkling of shells on soft substrates

Tomo Veldin[a], Boštjan Brank[b], Miha Brojan[a,*]

[a] Faculty of Mechanical Engineering, Laboratory for Nonlinear Mechanics, University of Ljubljana, Aškerčeva 6, Ljubljana SI-1000, Slovenia
[b] Faculty of Civil and Geodetic Engineering, University of Ljubljana, Jamova 2, Ljubljana SI-1000, Slovenia

ARTICLE INFO

Article history:
Received 24 March 2019
Revised 20 May 2019
Accepted 29 May 2019
Available online 30 May 2019

Keywords:
Surface wrinkling
Film-substrate composite
Model order reduction
Thin shells

ABSTRACT

We provide a robust finite element formulation for quantitative prediction of surface wrinkling of pressurized elastic shells on soft substrates. Our theory is build on three basic assumptions which involve thin shell kinematics, the approximation of the substrate response by a Winkler foundation and a model order reduction of the displacement field. Our element keeps all the nonlinear terms of the reduced model. The proposed formulation does not require any perturbations, either in the initial geometry or in the load, to incite the transition from fundamental to secondary equilibrium path for the considered set of shells, due to inherent asymmetric imperfections in the mesh. Numerical simulations using the derived element and an advanced path-following method on full spheres, hemispheres and spheroids show a very good quantitative agreement with theoretical predictions and experiments on the characteristic wavelength of the pattern as well as the qualitative depiction of the pattern evolution.

1. Introduction

Surface wrinkling is a mechanical instability that occurs when a thin flexible surface, bonded to a thick compliant substrate, is subjected to a critical compressive load. At this load, the initially smooth surface bifurcates from a state of homogeneous compression into a short wavelength periodic pattern that minimizes the elastic energy by local bending of the stiffer thin surface. The simplest example displaying this phenomenon is a beam on an elastic foundation, a model that was used in early studies to describe periodic buckling of railway tracks and buried pipelines (see e.g. the seminal works of Wieghardt [1], Biot [2] and Reissner [3]). Further research focused on the design of high-strength and light-weight elements for aircraft architecture and incited intensive studies on stability of sandwich panels in which the skins were modeled as plates and the core as a solid elastic medium (see e.g. Gough et al. [4] and Allen [5] for earlier investigations). Another strong impetus for intensive studies of wrinkling came quite recently, when it was recognized that periodic surface patterns may also exhibit many auspicious properties that can be exploited for advanced applications (see e.g. [6–13]). In both contexts – i.e., to either prevent the undesired wrinkling in engineering structures or to harness the auspicious properties of the surface pattern – a sound theoretical model, which is able to accurately predict the surface morphology at all load levels, is needed. It turns out that the complex response of the flexible-surface-soft-substrate system, due to e.g. strong geometric nonlinearities, wrinkling pattern transitions, large number of meta-stable states, complex equilibrium paths, etc., makes surface wrinkling a remarkably hard problem to solve for general shapes.

* Corresponding author.
E-mail address: miha.brojan@fs.uni-lj.si (M. Brojan).

https://doi.org/10.1016/j.cnsns.2019.104863
1007-5704/

Extensive experimental and theoretical studies have been done to explore the parameter space which controls the pattern formation on various sizes and shapes of substrates. It was shown that wrinkling pattern may be controlled by the ratios of Young's moduli of the film and the substrate, coefficients of thermal expansion, growth/swelling coefficients, etc. (depending on the external stress stimulus), film thickness, applied load, and the system's curvature. With the exception of curvature, the effects of these parameters are known today. For example, the relationship between the characteristic wavelength of the wrinkling pattern, and the material and geometric properties was discovered by Gough et al. [4] in 1940. More recently, the pattern selection mechanism for planar systems under equibiaxial loading was identified by Huang et al. [14] and Audoly and Boudaoud [15]. They found that the checkerboard pattern has the lowest energy just above the critical load, but soon after the load is increased further, the herringbone mode becomes the energy minimizer (see also Ref. [16]).

On the other hand, the available literature on wrinkling in curved systems still remains quite rare. Cao et al. [17] were the first to investigate wrinkling in this context on microscopic sized spheres subjected to temperature loading and discovered through experiments and numerical simulations by Abaqus [18] that spherical systems prefer hexagonal dimple patterns at lower over-stress, and the labyrinthine (herringbone-like) pattern at higher over-stress. Other micro-scale experiments on spherical surfaces by Breid and Crosby [19] and Yin et al. [20] as well as macro-scale experiments by Terwagne et al. [13] confirm these results. The fact that the curvature of the system does play an important role in pattern selection was also confirmed theoretically by Li et al. [21] and recently by Stoop et al. [22]. In their study, Li et al. [21] performed 3D finite element simulations (and another numerical analysis involving spherical harmonics) on a neoHookean hyperelastic bi-layer sphere wrinkled via volumetric shrinking. More general theoretical framework that simplifies the problem to radial displacement field by reduction of the Koiters elastic shell theory [23] to the Swift-Hohenberg fourth order equation was presented by Stoop et al. [22]. Their theory still preserves the essential geometric nonlinearities to display a quantitative description of the curvature-pattern interaction at low over-stress and predicts the same wrinkle modes as observed in previous studies [13,17,19–21].

Despite considerable research efforts, there are no simple and robust theoretical procedures able to accurately predict wrinkling in curved bi-layer composites. Most of the studies, among which many provide important physical insights (only a part of them is discussed above), are based on either simplified analytical procedures or numerical computations involving commercial finite element analysis software like Abaqus. The latter have in common that rather limited details are reported about used computational models. These include missing information about the type of elements, solution methods (linear buckling, nonlinear static, implicit or explicit dynamic, dynamic relaxation, inclusion of artificial viscous effects, etc.), boundary conditions, assumed imperfections and/or perturbation loads, arc-length procedures, branch switching, etc. It is thus very difficult to reproduce the reported results. Such studies use very fine meshes, thus making the surface wrinkling analysis extremely time consuming. In a lot of studies, a version of the 3D solid finite elements is used for both thin shell and substrate, see e.g. [26,42]. Another common way of shell-core modelling is adopting shell elements with rotational degrees of freedoms for the shell and 3D solid elements for the substrate, see e.g. [30,43]. It should be noted in this respect that representing the shell with one layer of solid elements, or coupling the shell and 3D solid elements without kinematic constraints, may induce large modeling errors.

Very few researchers develop their own numerical procedures. One of such studies is by Xu and Potier-Ferry [24] (see also the references to their previous work within that paper). They investigated the formation and evolution of the wrinkling pattern on a soft corestiff cylindrical shell subjected to axial compression. The numerical part of the analysis was based on a geometrically nonlinear 7-parameter shell model for the outer layer (see e.g. [34–36]), approximated with an 8-node geometrically nonlinear 3D-shell element with reduced integration, whereas the core was discretized with an 8-node linear 3D-solid element with reduced integration. Lagrange multipliers were applied to couple the corresponding nodal displacements at the interface between both materials. One of the main contributions of their work was the utilization of the asymptotic numerical method [25] to trace the post-buckling equilibrium and describe the phase diagram for the pattern modes of this highly nonlinear problem. A small perturbation force was imposed on the shell in order to initiate buckling. The computational model of Xu and Potier-Ferry was applied to flat and cylindrical shell-core systems [24]; they presented only one example with more complex geometry (a sphere) in [41].

In this work, we present a novel computational model for prediction of surface wrinkling on general curved shell-core systems subjected to pressure. Our theory offers a basis for a fast and robust numerical setup that can give a quantitative prediction of wrinkling patterns on curved shell-substrate systems. The theory is build upon three basic assumptions: (*i*) Because the outer layer is flexible and thin, the mechanical response of the shell-substrate system can be described by the nonlinear shell theory of Kirchhoff-Love type; (*ii*) The response of the substrate can be modelled via linear Winkler-type elastic foundation. A similar approach was used in studies by Zhao et al. [26] and Lagrange et al. [27] for cylindrical systems; (*iii*) To lower the complexity of this highly nonlinear problem but still preserving the fundamental features of the considered physical phenomena, we employ a model order reduction of the Kirchhoff-Love shell kinematics by assuming that the displacements tangential to the shell's surface can be neglected, because they are much smaller than the normal displacements. The same idea was adopted by Stoop et al. [22] in their study.

For the finite element discretization, we use quadrilateral finite element. Due to the requirement for the C^1 continuity of the displacement across the mesh, we apply the discrete-Kirchhoff approach. We design the element with three degrees of freedom per node, which are the normal displacement and two rotations of the shell normal, and apply the interpolations, which partially fulfill the Kirchhoff-Love constraint (i.e., the deformed shell director remains normal to the deformed mid-surface). The constraint is completely fulfilled at the nodes, unidirectionally fulfilled at the edges, and approximately fulfilled

at the Gauss points. The resulting shell quadrilateral has similar interpolations as the discrete-Kirchhoff quadrilateral for the plates, see e.g. Bohinc et al. [28,29], except that now the shell's curvature is taken into account. It should be noted that the derived finite element is not a general purpose finite element for shells (on elastic foundation) but it is a special-purpose finite element, designed for analysis of pressurized, curved shell-substrate systems. We name it DKQ-3 (as discrete-Kirchhoff quadrilateral with three degrees of freedom per node). The DKQ-3 has some interesting features: when flat it has one rigid body mode, but when curved it has zero rigid body modes. For this reason, the curved shell-substrate systems, such as spheres, half-spheres, spheroids, etc. can be analyzed with DKQ-3 without applying displacement-like boundary conditions. This resolves the problem of prescribed displacements in closed systems like spheres. Also, the second and the third nodal degrees of freedom (i.e., the rotations) are just the derivatives of the displacement. This enables large rotations of the shell to be naturally taken into account without any special treatment. It is also interesting to note that the present shell theory needs to be formulated in the manner of classical shell works, e.g. [40], resolving the displacement vector with respect to the surface base vectors. Such representation, which allows for a straightforward neglecting of the tangential displacements, is in contrast with the usual approach. Namely, it is common for a general shell theory, which constitutes a basis for a finite element formulation, to resolve the displacement vector with respect to the fixed Cartesian frame, see e.g. [37,38,47]; this considerably simplifies its numerical implementation.

We focus on wrinkling on spheres, spherical caps and spheroids. Note that our procedure is otherwise applicable to general curved shapes under pressure. In order to compute the equilibrium path, the path-following method from Stanić et al. [39] is applied. Because of the symmetries of the considered curved systems, each of them has clustered (multiple) stable bifurcation points at the critical pressure level at which the system buckles into wrinkling pattern mode. However, when these double curved surfaces are discretized by a random (yet fine) finite element mesh, the asymmetric imperfections are inevitably incorporated as there exists no mesh that could fully preserve the symmetries of the considered surfaces. Moreover, these imperfections dissipate clustered bifurcation points over a narrow region. This is just enough for the applied path-following procedure to pass the first bifurcation point without detecting it, because the stable bifurcation point vanishes due to asymmetric imperfections if small enough solution steps are prescribed. We note that in contrast to other numerical works, which all introduce small imperfections, either in the initial geometry or in the load, in order to perturb the system to be able to perform the transition from the fundamental equilibrium path to the secondary one, our numerical approach does not require such interventions. Very small imperfections, inevitably induced due to the mesh discretization, are enough for the used path-following method to switch to the secondary equilibrium path (at least for the considered double curved shells). After the first bifurcation point is passed, the solution is searched along the secondary branch. In some (rare) cases, the critical points were found on the secondary branch, which, however, were not studied further.

The rest of the paper is organized in the following way: in Section 2, the geometrically nonlinear reduced-order Kirchhoff-Love model for curved shell-substrate systems under external pressure is derived. In Section 3, we derive the corresponding discrete-Kirchhoff quadrilateral. Section 4 contains a set of illustrative numerical examples and the conclusions are drawn in Section 5.

2. Theoretical formulation

2.1. Basic assumptions

A thin elastic surface, which envelopes the soft core, will be modelled by the nonlinear Kirchhoff-Love (KL) shell theory. This theory is based on the kinematic assumption that the material fiber of the shell, which is initially normal to the mid-surface, remains straight and normal to the deformed mid-surface; thus, the effects of the transverse shear are neglected. It follows from this assumption that kinematic expressions for the initial (i.e., undeformed) and deformed configurations have the same structure. To distinguish between both configurations we mark the objects from the deformed configuration by a symbol $\tilde{\ }$, and the objects from the undeformed configuration without it.

We start the derivation of kinematic expressions by listing some fundamentals that are needed to structure the theory. The shell $\mathcal{S}$ will be parametrized as

$$\boldsymbol{x}(\theta^1,\theta^2,\theta^3) := {}_0\boldsymbol{x}(\theta^1,\theta^2) + \theta^3 \boldsymbol{a}_3(\theta^1,\theta^2), \tag{1}$$

where $(\theta^1, \theta^2, \theta^3)$ is a triplet of curvilinear (contravariant) coordinates, ${}_0\boldsymbol{x}$ is the parameterization of the shell's mid-surface $\mathcal{M}$, and $\boldsymbol{a}_3$ is the unit vector field, which is normal to $\mathcal{M}$. Here, the coordinate θ^3 measures the distance from $\mathcal{M}$ and is constrained by $\theta^3 \in [-t/2, t/2]$, where t denotes the thickness of the shell (t is constant in our case). The tangent space of $\mathcal{M}$ at a point on $\mathcal{T}_{\mathcal{M}}$ can be defined by a set of vector fields

$$\boldsymbol{a}_\alpha(\theta^1,\theta^2) := \frac{\partial\, {}_0\boldsymbol{x}(\theta^1,\theta^2)}{\partial\theta^\alpha} =: {}_0\boldsymbol{x}(\theta^1,\theta^2)_{,\alpha}\,, \qquad \alpha \in \{1,2\}, \tag{2}$$

which, together with

$$\boldsymbol{a}_3(\theta^1,\theta^2) := \frac{\boldsymbol{a}_1(\theta^1,\theta^2)\times\boldsymbol{a}_2(\theta^1,\theta^2)}{\|\boldsymbol{a}_1(\theta^1,\theta^2)\times\boldsymbol{a}_2(\theta^1,\theta^2)\|}, \tag{3}$$

constitute a local covariant basis $\{\boldsymbol{a}_1, \boldsymbol{a}_2, \boldsymbol{a}_3\}$ on $\mathcal{M}$. Note that here and in the rest of the paper we omit the functions' arguments for brevity and adopt the standard notation in Greek letters for index values from {1, 2} and Latin letters for

indices from {1, 2, 3}. Moreover, since $\boldsymbol{a}_3$ is perpendicular to $\mathcal{T}_{\mathcal{M}}$ and of unit length, then

$$\boldsymbol{a}_\alpha \cdot \boldsymbol{a}_3 = 0, \quad \boldsymbol{a}_{3,\alpha} \cdot \boldsymbol{a}_3 = 0, \quad \boldsymbol{a}_3 \cdot \boldsymbol{a}_3 = 1 \quad \text{and} \quad \boldsymbol{a}^3 = \boldsymbol{a}_3, \tag{4}$$

where the contravariant base vectors $\boldsymbol{a}^i$ are defined by the relation $\boldsymbol{a}^i \cdot \boldsymbol{a}_j = \delta^i_j$, and δ^i_j is Kronecker delta simbol. A similar local basis $\{\boldsymbol{g}_1, \boldsymbol{g}_2, \boldsymbol{g}_3\}$ can be constituted in $\mathcal{S}$ by differentiating Eq. (1),

$$\boldsymbol{g}_\alpha = \boldsymbol{a}_\alpha + \theta^3 \boldsymbol{a}_{3,\alpha} \quad \text{and} \quad \boldsymbol{g}_3 = \boldsymbol{a}_3. \tag{5}$$

Given by the inner product of the basis vectors, the corresponding covariant elements $g_{ij} := \boldsymbol{g}_i \cdot \boldsymbol{g}_j$ of the metric tensor $\boldsymbol{g}$ at a point in the shell $\mathcal{S}$ are:

$$g_{\alpha\beta} = a_{\alpha\beta} - 2\theta^3 b_{\alpha\beta} + (\theta^3)^2 c_{\alpha\beta}, \qquad g_{\alpha 3} = 0, \qquad g_{33} = 1, \tag{6}$$

where $a_{\alpha\beta}$, $b_{\alpha\beta}$ and $c_{\alpha\beta}$ represent the covariant elements of the first, second and third fundamental forms of the mid-surface $\mathcal{M}$, respectively:

$$a_{\alpha\beta} := \boldsymbol{a}_\alpha \cdot \boldsymbol{a}_\beta, \qquad b_{\alpha\beta} := -\boldsymbol{a}_\alpha \cdot \boldsymbol{a}_{3,\beta} = -\boldsymbol{a}_\beta \cdot \boldsymbol{a}_{3,\alpha} = \boldsymbol{a}_3 \cdot \boldsymbol{a}_{\alpha,\beta}\,, \qquad c_{\alpha\beta} := \boldsymbol{a}_{3,\alpha} \cdot \boldsymbol{a}_{3,\beta}\,. \tag{7}$$

For the measure of strain, we use the Green-Lagrange strain tensor $\boldsymbol{E} := (\tilde{\boldsymbol{g}} - \boldsymbol{g})/2$, where $\tilde{\boldsymbol{g}}$ denotes the metric tensor of the deformed shell configuration $\tilde{\mathcal{S}}$. As a consequence of the KL assumptions, the structure of all kinematic expressions from above remain the same for deformed configuration, with addition of $\tilde{}$ symbol on top of each object. Taking this into account, we can write the Green-Lagrange strain tensor components as

$$E_{\alpha\beta} = \epsilon_{\alpha\beta} + \theta^3 \kappa_{\alpha\beta} + (\theta^3)^2 \rho_{\alpha\beta}, \quad \text{and} \quad E_{i3} = 0, \tag{8}$$

where

$$\epsilon_{\alpha\beta} = \frac{1}{2}\left(\tilde{a}_{\alpha\beta} - a_{\alpha\beta}\right), \qquad \kappa_{\alpha\beta} = -(\tilde{b}_{\alpha\beta} - b_{\alpha\beta}), \qquad \rho_{\alpha\beta} = \frac{1}{2}\left(\tilde{c}_{\alpha\beta} - c_{\alpha\beta}\right). \tag{9}$$

Following the usual approach, see e.g. [37], we neglect the effect of $\rho_{\alpha\beta}$ in subsequent derivations, and relate the first and second fundamental forms corresponding to $\tilde{\mathcal{M}}$ to their counterparts from $\mathcal{M}$ via displacement vector field $\boldsymbol{u}$, defined by

$$\boldsymbol{u} := {}_0\tilde{\boldsymbol{x}} - {}_0\boldsymbol{x}. \tag{10}$$

Rearrangement and partial differentiation of Eq. (10) w.r.t. to θ^α yields

$$\tilde{\boldsymbol{a}}_\alpha = \boldsymbol{a}_\alpha + \boldsymbol{u}_{,\alpha}\,, \tag{11}$$

which leads to

$$\tilde{a}_{\alpha\beta} = \boldsymbol{u}_{,\alpha} \cdot \boldsymbol{u}_{,\beta} + \boldsymbol{u}_{,\alpha} \cdot \boldsymbol{a}_\beta + \boldsymbol{a}_\alpha \cdot \boldsymbol{u}_{,\beta} + \boldsymbol{a}_\alpha \cdot \boldsymbol{a}_\beta, \tag{12}$$

$$\tilde{b}_{\alpha\beta} = \tilde{\boldsymbol{a}}_3 \cdot \boldsymbol{a}_{\alpha,\beta} + \tilde{\boldsymbol{a}}_3 \cdot \boldsymbol{u}_{,\alpha\beta}\,. \tag{13}$$

With Eqs. (12) and (13) at hand, the membrane and bending strains from Eq. (9) become

$$\epsilon_{\alpha\beta} = \frac{1}{2}(\boldsymbol{u}_{,\alpha} \cdot \boldsymbol{u}_{,\beta} + \boldsymbol{u}_{,\alpha} \cdot \boldsymbol{a}_\beta + \boldsymbol{a}_\alpha \cdot \boldsymbol{u}_{,\beta}\,), \tag{14}$$

$$\kappa_{\alpha\beta} = -(\tilde{\boldsymbol{a}}_3 \cdot \boldsymbol{a}_{\alpha,\beta} + \tilde{\boldsymbol{a}}_3 \cdot \boldsymbol{u}_{,\alpha\beta} - b_{\alpha\beta}). \tag{15}$$

One can notice that if $\boldsymbol{u}$ is developed in the co- or contravariant basis of $\mathcal{T}_{\mathcal{M}}$, $\boldsymbol{u} = u^\alpha \boldsymbol{a}_\alpha + u^3 \boldsymbol{a}_3$ or $\boldsymbol{u} = u_\alpha \boldsymbol{a}^\alpha + u_3 \boldsymbol{a}^3$, respectively (as needed), then $\tilde{\boldsymbol{a}}_3$ is the only term from the deformed configuration at this stage.

2.2. Reduced kinematics

By neglecting the tangential components of the displacement field $\boldsymbol{u}$, such that $\boldsymbol{u} \approx u^3 \boldsymbol{a}_3 = u_3 \boldsymbol{a}^3$ and Eq. (4) $_4$, we can write $u^3 = u_3$ and

$$\boldsymbol{u} \approx u_3 \boldsymbol{a}_3. \tag{16}$$

Eqs. (14) and (15) thus reduce significantly, see [22].

Before we develop all the terms on the r.h.s. of expressions for the membrane and bending strains as functions of displacement u_3, we list some useful identities from differential geometry

$$\boldsymbol{a}_{3,\alpha} = -b^\gamma_\alpha \boldsymbol{a}_\gamma, \quad b^\gamma_\alpha a_{\gamma\beta} = b_{\alpha\beta}, \quad b^\gamma_\alpha b_{\gamma\beta} = c_{\alpha\beta}, \tag{17}$$

$$\boldsymbol{a}_1 \times \boldsymbol{a}_2 = \sqrt{a}\boldsymbol{a}_3, \quad \boldsymbol{a}_2 \times \boldsymbol{a}_3 = \sqrt{a}\boldsymbol{a}^1, \quad \boldsymbol{a}_3 \times \boldsymbol{a}_1 = \sqrt{a}\boldsymbol{a}^2, \tag{18}$$

$$a = \|\boldsymbol{a}_1 \times \boldsymbol{a}_2\|^2 = a_{11}a_{22} - (a_{12})^2, \quad \boldsymbol{a}^\alpha = a^{\alpha\gamma}\boldsymbol{a}_\gamma, \quad a^{\alpha\gamma}a_{\gamma\beta} = \delta^\alpha_\beta \tag{19}$$

$$\boldsymbol{a}_{\alpha,\beta} = \Gamma^\gamma_{\alpha\beta}\boldsymbol{a}_\gamma + b_{\alpha\beta}\boldsymbol{a}_3, \quad \Gamma^\gamma_{\alpha\beta} = \boldsymbol{a}^\gamma \cdot \boldsymbol{a}_{\alpha,\beta} = \boldsymbol{a}^\gamma \cdot \boldsymbol{a}_{\beta,\alpha} = -\boldsymbol{a}_\alpha \cdot \boldsymbol{a}^\gamma{}_{,\beta}\,, \tag{20}$$

where $\Gamma^\gamma_{\alpha\beta}$ are the Christoffel symbols of the second kind.

Let us rearrange the membrane strains. We use Eqs. (4) and (17) to differentiate (16) and get the following relations

$$\boldsymbol{u}_{,\alpha} = -u_3 b_\alpha^\gamma \boldsymbol{a}_\gamma + u_{3,\alpha}\,\boldsymbol{a}_3, \quad \boldsymbol{u}_{,\alpha}\cdot\boldsymbol{u}_{,\beta} = (u_3)^2 c_{\alpha\beta} + u_{3,\alpha}\,u_{3,\beta}\,, \quad \boldsymbol{a}_\alpha\cdot\boldsymbol{u}_{,\beta} = -u_3 b_{\alpha\beta}, \tag{21}$$

which are then inserted in Eq. (14) in order to obtain the reduced version of membrane strains $\epsilon_{\alpha\beta}$,

$$\epsilon_{\alpha\beta} = \frac{1}{2}\big((u_3)^2 c_{\alpha\beta} + u_{3,\alpha}\,u_{3,\beta}\,\big) - u_3 b_{\alpha\beta}. \tag{22}$$

In the same manner we express the reduced order of bending strains $\kappa_{\alpha\beta}$ in (15). We employ Eqs. (18) $_1$ and (11) to obtain

$$\sqrt{\tilde{a}}\tilde{\boldsymbol{a}}_3 = \boldsymbol{a}_1\times\boldsymbol{a}_2 + \boldsymbol{a}_1\times\boldsymbol{u}_{,2} + \boldsymbol{u}_{,1}\times\boldsymbol{a}_2 + \boldsymbol{u}_{,1}\times\boldsymbol{u}_{,2}\,. \tag{23}$$

Each term on the r.h.s. of (23) can be written as, see (21),

$$\boldsymbol{a}_1\times\boldsymbol{a}_2 = \sqrt{a}\boldsymbol{a}_3, \quad \boldsymbol{a}_1\times\boldsymbol{u}_{,2} = -\sqrt{a}(u_{3,2}\,\boldsymbol{a}^2 + u_3 b_2^2\boldsymbol{a}_3), \quad \boldsymbol{u}_{,1}\times\boldsymbol{a}_2 = -\sqrt{a}(u_{3,1}\,\boldsymbol{a}^1 + u_3 b_1^1\boldsymbol{a}_3), \tag{24}$$

$$\boldsymbol{u}_{,1}\times\boldsymbol{u}_{,2} = \sqrt{a}u_3\big((u_{3,1}\,b_2^2 - u_{3,2}\,b_1^2)\boldsymbol{a}^1 + (u_{3,2}\,b_1^1 - u_{3,1}\,b_2^1)\boldsymbol{a}^2 + u_3(b_1^1 b_2^2 - b_1^2 b_2^1)\boldsymbol{a}_3\big). \tag{25}$$

Furthermore, $\sqrt{\tilde{a}}$ can be expressed via Eqs. $(19)_1$, $(7)_1$, (11), $(21)_3$ in the following form

$$\tilde{a} = \tilde{a}_{11}\tilde{a}_{22} - (\tilde{a}_{12})^2, \tag{26}$$

where

$$\tilde{a}_{11} = a_{11} - 2u_3 b_{11} + (u_3)^2 c_{11} + (u_{3,1}\,)^2 \tag{27}$$

$$\tilde{a}_{22} = a_{22} - 2u_3 b_{22} + (u_3)^2 c_{22} + (u_{3,2}\,)^2 \tag{28}$$

$$\tilde{a}_{12} = a_{12} - 2u_3 b_{12} + (u_3)^2 c_{12} + u_{3,1}\,u_{3,2}\,. \tag{29}$$

The term $\boldsymbol{u}_{,\alpha\beta}$ in Eq. (15) is expanded with the help of identities $(17)_1$ and (20) as

$$\boldsymbol{u}_{,\alpha\beta} = (-u_{3,\beta}\,b_\alpha^\gamma - u_3 b_{\alpha,\beta}^\gamma - u_3 b_\alpha^\lambda \Gamma_{\lambda\beta}^\gamma - u_{3,\alpha}\,b_\beta^\gamma)\boldsymbol{a}_\gamma + (u_{3,\alpha\beta} - u_3 c_{\alpha\beta})\boldsymbol{a}_3. \tag{30}$$

Finally, one can employ Eqs. (23)–(30) to evaluate the dot products

$$\tilde{\boldsymbol{a}}_3\cdot\boldsymbol{a}_{\alpha,\beta} = \sqrt{\frac{a}{\tilde{a}}}\big(\widehat{A}\Gamma_{\alpha\beta}^1 + \widehat{B}\Gamma_{\alpha\beta}^2 + \widehat{C}b_{\alpha\beta}\big) \tag{31}$$

and

$$\begin{aligned}\tilde{\boldsymbol{a}}_3\cdot\boldsymbol{u}_{,\alpha\beta} = \sqrt{\frac{a}{\tilde{a}}}\big(&\widehat{A}(-u_{3,\beta}b_\alpha^1 - u_3 b_{\alpha,\beta}^1 - u_3 b_\alpha^\omega\Gamma_{\omega\beta}^1 - u_{3,\alpha}b_\beta^1)\\ &+\widehat{B}(-u_{3,\beta}b_\alpha^2 - u_3 b_{\alpha,\beta}^2 - u_3 b_\alpha^\omega\Gamma_{\omega\beta}^2 - u_{3,\alpha}b_\beta^2) + \widehat{C}(-u_3 c_{\alpha\beta} + u_{3,\alpha\beta})\big),\end{aligned} \tag{32}$$

where

$$\widehat{A} = (-u_3 u_{3,2}b_1^2 + u_3 u_{3,1}b_2^2 - u_{3,1}), \tag{33}$$

$$\widehat{B} = (-u_3 u_{3,1}b_2^1 + u_3 u_{3,2}b_1^1 - u_{3,2}) \tag{34}$$

$$\widehat{C} = (1 - u_3 b_2^2 - u_3 b_1^1 + (u_3)^2 b_1^1 b_2^2 - (u_3)^2 b_1^2 b_2^1), \tag{35}$$

necessary to express the bending strains $\kappa_{\alpha\beta}$ in (15) as functions of displacement u_3.

The expression for bending strains is quite complex. For comparison, let us write the expression for linear bending strains, which is much simpler

$$\kappa_{\alpha\beta} = -u_{3,\alpha\beta} + u_3 c_{\alpha\beta} + u_{3,\gamma}\,\Gamma_{\alpha\beta}^\gamma. \tag{36}$$

2.3. Potential energy

The total potential energy functional for our system is

$$\Pi(u_3) = \int_{\mathcal{M}}\big({}_0W(\epsilon_{\alpha\beta}) + {}_1W(\kappa_{\alpha\beta})\big)dA - \int_{\mathcal{M}}\left(pu_3 - \frac{K_s}{2}(u_3)^2\right)dA, \tag{37}$$

where ${}_0W$ and ${}_1W$ are the membrane and bending strain energy functions, respectively, p is surface pressure acting in the direction of $-\boldsymbol{a}_3$, K_s is the stiffness of area spring representing substrate reaction, and $\mathcal{M}$ denotes the undeformed shell's mid-surface, as before. Membrane forces and bending moments are defined as

$$n_{\alpha\beta} = \frac{\partial_0 W(\epsilon_{\alpha\beta})}{\partial\epsilon_{\alpha\beta}}, \qquad m_{\alpha\beta} = \frac{\partial_1 W(\kappa_{\alpha\beta})}{\partial\kappa_{\alpha\beta}}. \tag{38}$$

Equilibrium of the mechanical system is sought through minimization of the potential energy functional Π. The necessary condition for its minimum is

$$\delta\Pi = \frac{d}{d\varepsilon}\big[\Pi(u_3 + \varepsilon\delta u_3)\big]\Big|_{\varepsilon=0} = 0, \tag{39}$$

where $\delta\Pi$ denotes the first variation of the potential energy, ε is a scalar parameter and δu_3 is kinematically admissible variation of the displacement field. By applying formalism (39) in Eq. (37) one gets

$$\delta\Pi(u_3, \delta u_3) = \int_{\mathcal{M}} (\delta\epsilon_{\alpha\beta} n_{\alpha\beta} + \delta\kappa_{\alpha\beta} m_{\alpha\beta}) dA - \int_{\mathcal{M}} (\delta u_3 p - \delta u_3 K_s u_3) dA = 0, \tag{40}$$

where $\delta\epsilon_{\alpha\beta}$ and $\delta\kappa_{\alpha\beta}$ are kinematically admissible variations of membrane and bending strains, respectively.

2.4. Constitutive relations

We will use the thin-shell version of the isotropic St. Venant-Kirchhoff hyperelastic strain energy function. This particular strain energy function is appropriate for large displacements and small strains, which is the case for the problem under consideration. The thin-shell version takes into account the plane stress assumption. It is defined as a sum of two parts $W = {}_0W + {}_1W$, the first representing shell membrane deformation energy density and the second shell bending deformation energy density. For the chosen shell strain energy function, the membrane forces and bending moments are

$$n^{\alpha\beta} = \frac{Et}{1-\nu^2} H^{\alpha\beta\gamma\delta}\epsilon_{\alpha\beta}, \qquad m^{\alpha\beta} = \frac{Et^3}{12(1-\nu^2)} H^{\alpha\beta\gamma\delta}\kappa_{\alpha\beta}, \tag{41}$$

where E is the Young's modulus, ν is the Poisson's ratio and $H^{\alpha\beta\gamma\delta}$ are the components of the isotropic constitutive tensor,

$$H^{\alpha\beta\gamma\delta} = \nu a^{\alpha\beta} a^{\gamma\delta} + \frac{1}{2}(1-\nu)\big(a^{\alpha\gamma} a^{\beta\delta} + a^{\alpha\delta} a^{\beta\gamma}\big). \tag{42}$$

Let us use the Voigt notation for strains and stress resultants

$$[\boldsymbol{\epsilon}] = \big[\epsilon_{11}, \epsilon_{22}, 2\epsilon_{12}\big]^T, \qquad [\boldsymbol{\kappa}] = \big[\kappa_{11}, \kappa_{22}, 2\kappa_{12}\big]^T, \tag{43}$$

$$[\boldsymbol{n}] = \big[n^{11}, n^{22}, n^{12}\big]^T, \qquad [\boldsymbol{m}] = \big[m^{11}, m^{22}, m^{12}\big]^T. \tag{44}$$

The relations between these vectors are $\boldsymbol{n} = \frac{Et}{1-\nu^2}\boldsymbol{H}\boldsymbol{\epsilon}$ and $\boldsymbol{m} = \frac{Et^3}{12(1-\nu^2)}\boldsymbol{H}\boldsymbol{\kappa}$, where the constitutive tensor $\boldsymbol{H}$ is represented as, see e.g. [37],

$$[\boldsymbol{H}] = \begin{bmatrix} a^{11}a^{11} & \nu a^{11}a^{22} + (1-\nu)a^{12}a^{12} & a^{11}a^{12} \\ \nu a^{11}a^{22} + (1-\nu)a^{12}a^{12} & a^{22}a^{22} & a^{22}a^{12} \\ a^{11}a^{12} & a^{22}a^{12} & \frac{1-\nu}{2}a^{11}a^{22} + \frac{1+\nu}{2}a^{12}a^{12} \end{bmatrix}. \tag{45}$$

With this notation at hand, we can rewrite the minimum of the potential energy (40) for the Kirchhoff-Love shell on elastic foundation that is subjected to pressure p as

$$\delta\Pi(u_3, \delta u_3) = \int_{\mathcal{M}} \frac{Et}{1-\nu^2}\big(\delta\boldsymbol{\epsilon}\cdot\boldsymbol{H}\boldsymbol{\epsilon} + \frac{t^2}{12}\delta\boldsymbol{\kappa}\cdot\boldsymbol{H}\boldsymbol{\kappa}\big) dA + \int_{\mathcal{M}} \delta u_3 K_s u_3 dA - \int_{\mathcal{M}} \delta u_3 p dA = 0. \tag{46}$$

where $[\delta\boldsymbol{\epsilon}] = [\delta\epsilon_{11}, \delta\epsilon_{22}, 2\delta\epsilon_{12}]^T$ and $[\delta\boldsymbol{\kappa}] = [\delta\kappa_{11}, \delta\kappa_{22}, 2\delta\kappa_{12}]^T$.

3. Reduced-order discrete-Kirchhoff quadrilateral

3.1. Approximation of initial surface geometry

Let the initial shell mid-surface $\mathcal{M}$ be discretized by N_{el} non-overlapping quadrilateral finite elements with 4 nodes, such that $\mathcal{M} \approx \bigcup_{e=1}^{N_{el}} \mathcal{M}^e$. The domain $\mathcal{M}^e$ (the initial geometry of the element) and the field of its normal are defined by the following approximations

$${}_0\boldsymbol{x}(\xi, \eta) = \sum_{I=1}^{4} N_I(\xi, \eta)\, {}_0\boldsymbol{x}_I, \qquad \boldsymbol{a}_3(\xi, \eta) = \sum_{I=1}^{4} N_a(\xi, \eta)\boldsymbol{a}_{3I}. \tag{47}$$

where ${}_0\boldsymbol{x}_I$ and $\boldsymbol{a}_{3I}$ are coordinates and surface normal at node I, respectively, whereas ξ and η are the coordinates that are interpreted as $\xi = \theta^1$ and $\eta = \theta^2$ over $\mathcal{M}_e$, and N_I are bi-linear Lagrange interpolation functions defined over the bi-unit square $[-1, 1] \times [-1, 1]$,

$$N_1 = \frac{1}{4}(1-\xi)(1-\eta), \quad N_2 = \frac{1}{4}(1+\xi)(1-\eta), \quad N_3 = \frac{1}{4}(1+\xi)(1+\eta), \quad N_4 = \frac{1}{4}(1-\xi)(1+\eta). \tag{48}$$

Interpolations (47) are used for approximation of geometric terms, which appear in expressions for $\epsilon_{\alpha\beta}$ and $\kappa_{\alpha\beta}$ (i.e., the components of the first, second and third fundamental forms, etc.), over the element.

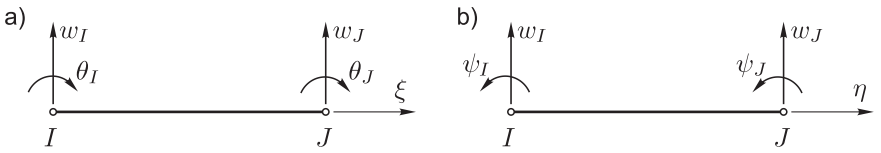

Fig. 1. (a) Nodal parameters for edges 12 and 43. (b) Nodal parameters for edges 23 and 14.

3.2. Interpolations of displacement and rotation fields

In the rest of this section, we will use the notation $w := u_3$ to avoid complicated indexing. Moreover, we will approximate $u_{3,1}$ with rotation $-\theta$, and $u_{3,2}$ with rotation ψ.

3.2.1. Interploations along element's edges

Let us first design interpolations along the four edges of the element; we will use the following notation: the first node of the edge IJ is I and the second node is J. Let us start with $IJ = 12$ and $IJ = 43$. For these two edges, we will consider displacement w and rotation θ, see Fig. 1a). We choose cubic interpolation for displacement and quadratic interpolation for rotation along the edge

$$w^{IJ} = w_I N_I + w_J N_J + \sum_{b=3}^{4} \hat{w}_b^{IJ} \bar{N}_b, \quad \theta^{IJ} = \theta_I N_I + \theta_J N_J + \hat{\theta}^{IJ} \bar{N}_3, \quad IJ \in \{12, 43\}, \tag{49}$$

where $N_I = (1-\xi)/2$, $N_J = (1+\xi)/2$ are the interpolation functions (48) along the considered edges with $\eta = -1$ and $\eta = 1$, respectively, and $\bar{N}_3 = 1-\xi^2$, $\bar{N}_4 = \xi(1-\xi^2)$. Only two nodal displacements, w_I, w_J, and two nodal rotations, θ_I, θ_J, are the acceptable parameters for our element in Eq. (49). The other parameters in Eq. (49) are condensed out by enforcing the KL normality hypothesis, which can be expressed as $\partial w^{IJ}/\partial\xi + \theta^{IJ} = 0$. Setting the constant, linear and quadratic terms of the normality constraint to zero, results in

$$\hat{w}_3^{IJ} = \frac{L}{8}(\theta_J - \theta_I), \quad \hat{w}_4^{IJ} = \frac{L}{4}\left(\frac{w_J - w_I}{L} + \frac{1}{2}(\theta_I + \theta_J)\right), \quad \hat{\theta}^{IJ} = -\frac{6}{L}\hat{w}_4^{IJ}, \tag{50}$$

where $IJ \in \{12, 43\}$. By plugging in the edge length of the bi-unit square, $L = 2$, and Eq. (50) into (49), we get a four-parameter linked interpolations for displacement w and rotation θ along the edges $IJ = 12$ and $IJ = 43$.

For the two edges $IJ = 23$ and $IJ = 14$, we will consider displacement w and rotation ψ, see Fig. 1b. We choose the following interpolations

$$w^{IJ} = w_I N_I + w_J N_J + \sum_{b=3}^{4} \hat{w}_b^{IJ} \bar{\bar{N}}_b, \quad \psi^{IJ} = \psi_I N_I + \psi_J N_J + \hat{\psi}^{IJ} \bar{\bar{N}}_3, \quad IJ \in \{23, 14\}, \tag{51}$$

where $N_I = (1-\eta)/2$, $N_J = (1+\eta)/2$ are the interpolation functions (48) along the considered edges with $\xi = 1$ and $\xi = -1$, respectively, and $\bar{\bar{N}}_3 = 1-\eta^2$, $\bar{\bar{N}}_4 = \eta(1-\eta^2)$. By enforcing the KL normality hypothesis along the edges, which is $\partial w^{IJ}/\partial\eta - \psi^{IJ} = 0$, we get

$$\hat{w}_3^{IJ} = \frac{L}{8}(\psi_I - \psi_J), \quad \hat{w}_4^{IJ} = \frac{L}{4}\left(\frac{w_J - w_I}{L} - \frac{1}{2}(\psi_I + \psi_J)\right), \quad \hat{\psi}^{IJ} = \frac{6}{L}\hat{w}_4^{IJ}, \tag{52}$$

where $IJ \in \{23, 14\}$. Similarly as before, plugging Eq. (52) and $L = 2$ into (51), yields linked interpolations for displacement w and rotation ψ along the edges $IJ = 23$ and $IJ = 14$.

The above interpolations satisfy the KL normality constraint along each quadrilateral's edge, but only in the direction of the edge. However, at element's nodes (at cross-sections of edges), the KL normality constraint is fully satisfied.

3.2.2. Interpolations over the element

Let us design interpolations over the element in such a way that they coincide at element's edges with the expressions given in Eqs. (49)–(52). This is achieved if displacement and rotations are interpolated over the element as

$$w = \sum_{I=1}^{4} N_I w_I + \sum_{IJ} \left(N_{IJ}\hat{w}_3^{IJ} + M_{IJ}\hat{w}_4^{IJ}\right), \tag{53}$$

$$\theta = \sum_{I=1}^{4} N_I \theta_I + N_{12}\hat{\theta}^{12} + N_{43}\hat{\theta}^{43}, \tag{54}$$

$$\psi = \sum_{I=1}^{4} N_I \psi_I + N_{23}\hat{\psi}^{23} + N_{14}\hat{\psi}^{14}, \tag{55}$$

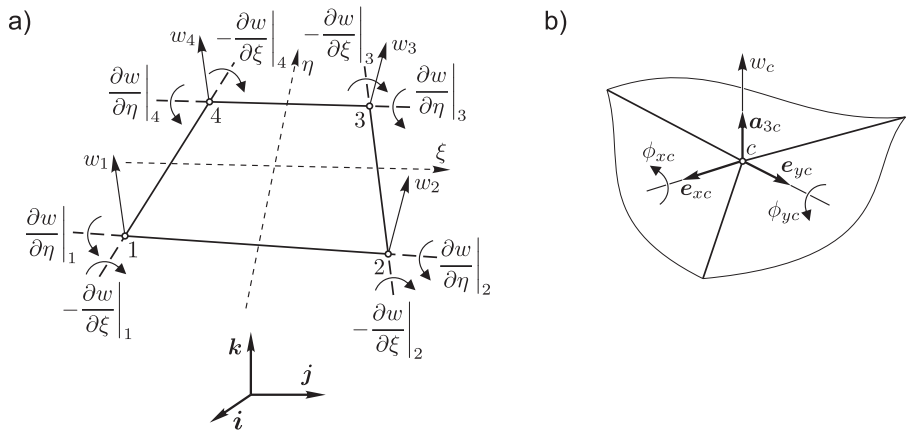

Fig. 2. (a) Nodal parameters interpolated over the element. (b) Degrees of freedom at a node..

where $IJ = \{12, 23, 43, 14\}$, the expressions for $\hat{w}_3^{IJ}$, $\hat{w}_4^{IJ}$, $\hat{\theta}^{IJ}$, and $\hat{\psi}^{IJ}$ are given in Eqs. (50) and (52), and the interpolation functions are

$$N_{12} = (1-\eta-\xi^2+\xi^2\eta)/2, \qquad N_{23} = (1+\xi-\eta^2-\xi\eta^2)/2,$$
$$N_{43} = (1+\eta-\xi^2-\xi^2\eta)/2, \qquad N_{14} = (1-\xi-\eta^2+\xi\eta^2)/2, \tag{56}$$

$$M_{12} = (\xi-\xi\eta-\xi^3+\xi^3\eta)/2, \qquad M_{23} = (\eta+\xi\eta-\eta^3-\xi\eta^3)/2,$$
$$M_{43} = (-\xi-\xi\eta+\xi^3+\xi^3\eta)/2, \qquad M_{14} = (-\eta+\xi\eta+\eta^3-\xi\eta^3)/2. \tag{57}$$

The rotations θ and ψ in Eqs. (54) and (55) are close approximations of the displacement derivatives, because

$$\theta = \begin{cases} -\partial w/\partial\xi \ : \text{at all nodes and edges } IJ \in \{12, 43\}\ , \\ \approx -\partial w/\partial\xi \ : \text{otherwise}, \end{cases} \tag{58}$$

$$\psi = \begin{cases} \partial w/\partial\eta \ : \text{at all nodes and edges } IJ \in \{23, 14\}\ , \\ \approx \partial w/\partial\eta \ : \text{otherwise}, \end{cases} \tag{59}$$

which is illustrated in Fig. 2(a).

3.2.3. Transformation at nodes

The nodal rotations, $\theta_I = -\partial w/\partial\xi\ |_I$ and $\psi_I = \partial w/\partial\eta\ |_I$ we introduced above, have a local (i.e., element) character, and cannot be used as degrees of freedom. They are not unique at the node of the mesh. In order to define nodal degrees of freedom, we construct a local orthonormal basis at each node of the mesh. At node c such a basis is $\{\boldsymbol{e}_{xc}, \boldsymbol{e}_{yc}, \boldsymbol{a}_{3c}\}$, where $\boldsymbol{a}_{3c}$ is mid-surface normal at that point, see Fig. 2(b). This basis is unique for all the elements meeting at node c, so that the nodal degrees of freedom can be defined as: displacement w_c, rotation around $\boldsymbol{e}_{xc}$, denoted a $\phi_{xc} = \partial w/\partial y\ |_c$, and rotation around $\boldsymbol{e}_{yc}$, denoted as $\phi_{yc} = -\partial w/\partial x\ |_c$. Here, x and y are Cartesian coordinates that span the tangential plane to the mid-surface at c and have directions of $\boldsymbol{e}_{xc}$ and $\boldsymbol{e}_{yc}$, respectively.

The transformation between the element nodal rotations θ_I, ψ_I and the nodal degrees of freedom ϕ_{xc}, ϕ_{yc} is needed (for I and c denoting the same node in space). It follows from the chain rule that

$$\left.\frac{\partial w}{\partial \boldsymbol{\xi}}\right|_I = \left.\frac{\partial w}{\partial x}\right|_c \left.\frac{\partial x}{\partial_0 \boldsymbol{x}}\right|_c \cdot \left.\frac{\partial_0 \boldsymbol{x}}{\partial \boldsymbol{\xi}}\right|_I + \left.\frac{\partial w}{\partial y}\right|_c \left.\frac{\partial y}{\partial_0 \boldsymbol{x}}\right|_c \cdot \left.\frac{\partial_0 \boldsymbol{x}}{\partial \boldsymbol{\xi}}\right|_I, \quad [\boldsymbol{\xi}] = [\xi, \eta]. \tag{60}$$

Because $\partial x/\partial_0\boldsymbol{x}\ |_c = \boldsymbol{e}_{xc}$, $\partial y/\partial_0\boldsymbol{x}\ |_c = \boldsymbol{e}_{yc}$, $\partial_0\boldsymbol{x}/\partial\xi\ |_I = \boldsymbol{a}_{1I}$, and $\partial_0\boldsymbol{x}/\partial\eta\ |_I = \boldsymbol{a}_{2I}$, one gets the following transformation rule

$$\begin{bmatrix} \theta_I \\ \psi_I \end{bmatrix} = \begin{bmatrix} \boldsymbol{e}_{xc}\cdot\boldsymbol{a}_{1I} & -\boldsymbol{e}_{yc}\cdot\boldsymbol{a}_{1I} \\ -\boldsymbol{e}_{xc}\cdot\boldsymbol{a}_{2I} & \boldsymbol{e}_{yc}\cdot\boldsymbol{a}_{2I} \end{bmatrix} \begin{bmatrix} \phi_{y_c} \\ \phi_{x_c} \end{bmatrix}. \tag{61}$$

When the transformation (61) is inserted in Eqs. (53)–(55), the element displacement w and rotations θ and ψ become functions of the element's degrees of freedom, which are w_I, ϕ_{x_I} and ϕ_{y_I}, $I \in \{1, \ldots, 4\}$. With this, the interpolation of displacement and its derivatives over the element is complete. It is now straightforward to express the membrane and bending strains by the element's degrees of freedom.

3.3. Assumed natural strain formulation

The interpolations for displacement and rotations chosen above give zero transverse shear strains, $\gamma_\xi = \gamma_\eta = 0$, only at the element nodes. The shear strain $\gamma_\xi = \partial w/\partial\xi + \theta$ is zero also along the edges $IJ = 12$ and $IJ = 43$, and the shear strain $\gamma_\eta = \partial w/\partial\eta - \psi$ is zero along the edges $IJ = 23$ and $IJ = 14$. Thus, the transverse shear strains do not vanish throughout the element. For this reason, we apply the assumed natural strain (ANS) concept for the transverse shear interpolation

$$\boldsymbol{\gamma}^* = \sum_{I=1}^{4} N_I \boldsymbol{\gamma}_I, \quad [\boldsymbol{\gamma}] = [\gamma_\xi, \gamma_\eta]^T, \tag{62}$$

where $\boldsymbol{\gamma}^* = \mathbf{0}$, because nodal transverse shear strains are zero.

The variational framework for the ANS concept is the Hu-Washizu functional [44]. For the considered problem, it has the following form for an element

$$\begin{aligned} \Pi^e_{HW}(w, \theta, \psi, \boldsymbol{\gamma}^*, \boldsymbol{\tau}) = & \int_{\mathcal{M}^e} \left(\frac{Et}{2(1-\nu^2)} \left(\boldsymbol{\epsilon} \cdot \boldsymbol{H}\boldsymbol{\epsilon} + \frac{t^2}{12} \boldsymbol{\kappa} \cdot \boldsymbol{H}\boldsymbol{\kappa} \right) + \boldsymbol{\tau}(\boldsymbol{\gamma}^* - \boldsymbol{\gamma}) \right) dA^e \\ & - \int_{\mathcal{M}^e} \left(pw - \frac{1}{2} K_s (w)^2 \right) dA^e, \end{aligned} \tag{63}$$

where $\boldsymbol{\epsilon}$, $\boldsymbol{\kappa}$, and $\boldsymbol{\gamma}$ are the membrane, bending and transverse shear strains, respectively, evaluated by w, θ and ψ from (53)–(55), and $\boldsymbol{\tau}$ are transverse shear forces. Let us assume that $\boldsymbol{\tau}$ is orthogonal to $\boldsymbol{\gamma}$. In this case, the transverse shear drops out, and the Hu-Washizu functional reduces to standard potential energy functional

$$\Pi^e(w, \theta, \psi) = \int_{\mathcal{M}^e} \left(\frac{Et}{2(1-\nu^2)} \left(\boldsymbol{\epsilon} \cdot \boldsymbol{H}\boldsymbol{\epsilon} + \frac{t^2}{12} \boldsymbol{\kappa} \cdot \boldsymbol{H}\boldsymbol{\kappa} \right) \right) dA^e - \int_{\mathcal{M}^e} \left(pw - \frac{1}{2} K_s (w)^2 \right) dA^e. \tag{64}$$

The above assumption implies that the variationally consistent shear forces are only those orthogonal to $\boldsymbol{\gamma}$.

The discretized form of the potential energy for the considered problem and its variation (related to equilibrium) can now be written as

$$\Pi = \mathbb{A}_e^{N_{el}} \Pi^e, \quad \delta\Pi = \mathbb{A}_e^{N_{el}} \delta\Pi^e = 0, \tag{65}$$

where $\mathbb{A}$ is a finite element assembly operator.

3.4. Variation and linearization

When the interpolations (47)–(53) and transformation (49) are inserted into the potential energy functional (65) and the variation of the latter is performed in order to find its minimum, a system of highly non-linear equations is obtained, with the nodal degrees of freedom as the unknowns. In order to solve this system of equations by incremental-iterative Newton-Raphson procedure (which is a part in the applied path-following method), the equations have to be consistently linearized. We note that the element's contribution to the system follows from the variation of (64) (and the assembly operator). We omit the details of the variation of the element's potential energy (64) and the linearization of the resulting set of the element's nonlinear equations. We note, however, that we performed the variation and linearization by applying Mathematica [46], its add-on AceGen [45] and that the derived finite element was implemented in the AceFEM [45] computer code. The element's integrals were computed by a 2×2 Gauss integration rule.

4. Numerical examples

In this section, we present the results of our numerical simulations on a full sphere, a hemisphere and a spheroid shell-substrate composites. The outer shell surface was subjected to constant pressure, while the inner shell surface was supported by a substrate, which was modelled as a linear Winkler-type elastic foundation. The modulus of elastic foundation K_s was calculated from Eq. (B.10) in Ref [27]., which was originally developed for a cylinder. Note that a similar formula developed for flat systems (see Eq. (B.11) in Ref. [27]), and another formula developed for cylinders (Eq. (11) in Ref. [26]), give practically the same result for K_s for our set of geometric and material parameters (the relative difference is on average around 0.5 %). All analyses were carried out by using a path-following method described in [39].

4.1. Membrane test

Before presenting the results, let us show how the derived finite element describes pure linear membrane deformations. Fig. 3 shows two variants of a 3×3 element mesh for a cylindrical patch, a symmetry preserving and a distorted one, both subjected to the same load. The rotations were restrained along all edges of the patch. The results on a symmetry preserving mesh in Fig. 3a perfectly match the exact analytical solution $u_3 = 0.04$ mm for radial displacement for all the nodes. On

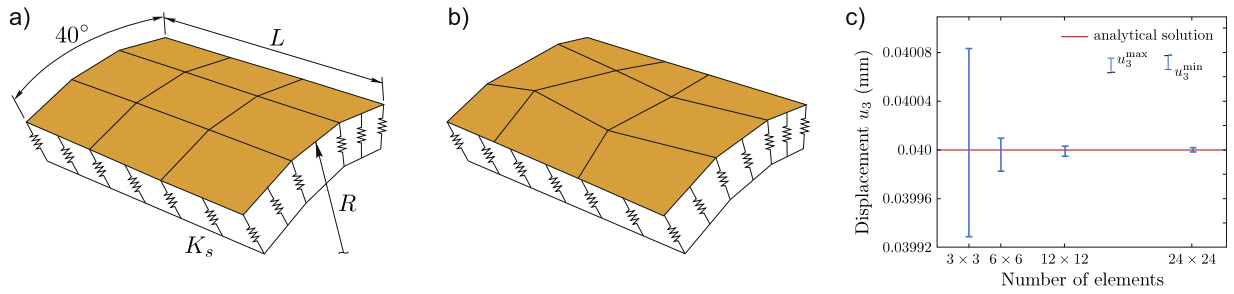

Fig. 3. Mesh on a 40° cylindrical patch: (a) Symmetry preserving regular mesh, (b) Distorted mesh. (c) Convergence diagram for the distorted mesh: min. and max. displacement u_3 as a function of mesh size. The following parameters were used: radius of the patch $R = 20$ mm, length $L = 20$ mm, thickness $t = 0.1$ mm, Young's modulus $E = 10^6$ MPa, Poisson ratio $\nu = 0$, spring constant $K_s = 0$ and pressure load $p = 10$ MPa.

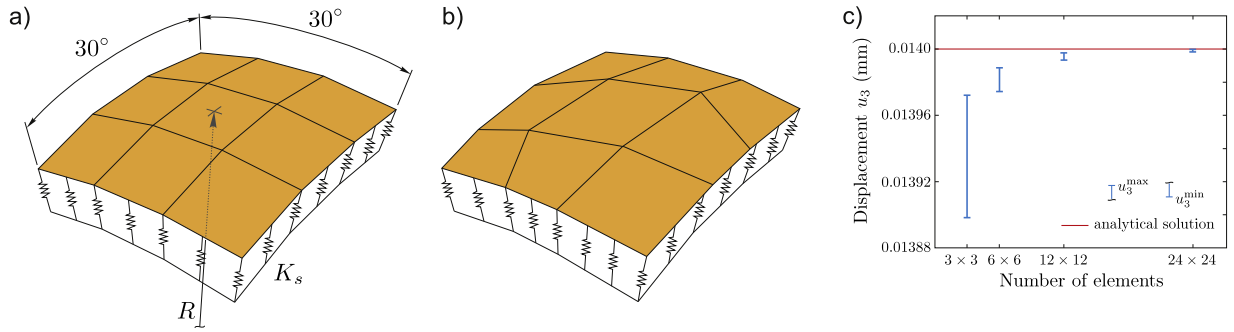

Fig. 4. Mesh on a $30° \times 30°$ spherical patch: (a) Regular mesh, (b) Distorted mesh. (c) Convergence diagram for the distorted mesh: min. and max. displacement u_3 as a function of mesh size. The following parameters were used: radius of the patch $R = 20$ mm, thickness $t = 0.1$ mm, Young modulus $E = 10^6$ MPa, Poisson ratio $\nu = 0.3$, spring constant $K_s = 0$ and pressure load $p = 10$ MPa.

the other hand, the distorted mesh in Fig. 3b yields slightly different nodal displacements in the range $u_3 \in [0.039929, 0.040083]$ mm, which is due to induced asymmetric imperfections. To illustrate the convergence of the solution on the distorted mesh, we plot in Fig. 3c four vertical bars (in blue color), corresponding to the difference between the maximal and minimal displacement u_3 calculated on each of the four meshes. For comparison, a mesh with 24×24 elements yields nodal displacements in the range $u_3 \in [0.0399984, 0.0400019]$ mm.

Because no symmetry preserving quadrilateral mesh exists for a spherical patch, both meshes in Fig. 4 introduce symmetry breaking imperfections. Therefore, we obtain slightly different nodal radial displacements in both cases, which are very close to the analytical solution 0.014 mm, though. The two meshes (a) and (b) yield $u_3 \in [0.013929, 0.013940]$ mm and $u_3 \in [0.013898, 0.013972]$ mm, respectively. Again, both rotations were restrained along the edges. A convergence plot for a distorted mesh on the spherical patch is shown in Fig. 4c. Similar to the cylindrical case the difference becomes smaller as the mesh is refined. For comparison to the 3×3 mesh, a mesh with 24×24 elements yields nodal displacements in the range $u_3 \in [0.0139982, 0.0139997]$ mm.

4.2. Spherical shell

A spherical shell, with geometric and material properties given in the caption of Fig. 5, was pressurized by an external radial pressure p. As shown in Fig. 5, the pressure induces the change of the normal displacement and the surface pattern. The normal displacement u_3 was traced at a node located at the center of (or the closest to) a generic dimple.

In the initial stage, where u_3 varies linearly with p, large solution increments were allowed. At some increment, several negative pivots were found for the equilibrium tangent stiffness matrix at that load level. This was an indication that several critical points in a cluster of stable bifurcation points (as generically illustrated in Fig. 6a, see also e.g. [48]) were passed. Clustered bifurcation points are typical for discretized problems with multiple symmetries, see e.g. [48]. Hence, a step-back to the previous equilibrium configuration was done and the analysis proceeded with smaller solution increments, which ensured a smooth transition from the primary to the secondary equilibrium path, see Fig. 6b.

This way, the applied path-following procedure passed the first bifurcation point without detecting it, because the stable bifurcation point vanished due to asymmetric imperfections induced by the mesh, see e.g. [49]. These imperfections are clearly visible already on the first deformed configuration in Fig. 5 as very small non-homogeneity of normal displacement.

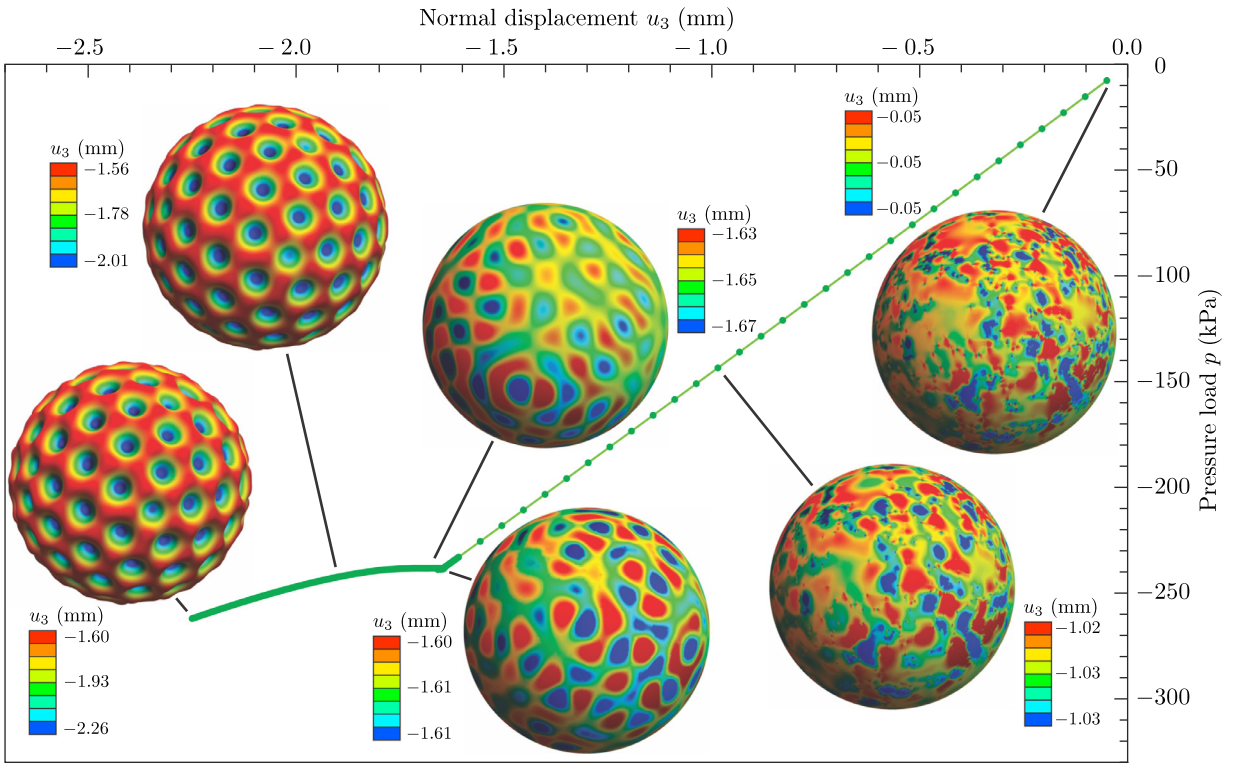

Fig. 5. Development of the normal displacement field u_3 on a spherical shell as the pressure load p is increased. Geometrical and material parameters are as follows: radius $R = 20.0$ mm, thickness $t = 0.8$ mm, Young's modulus $E = 2.1$ MPa, Poisson's ratio $\nu = 0.49$, modulus of elastic foundation $K_s = 0.1302$ N/mm^3, and the number of elements in the mesh $n = 148\,512$.

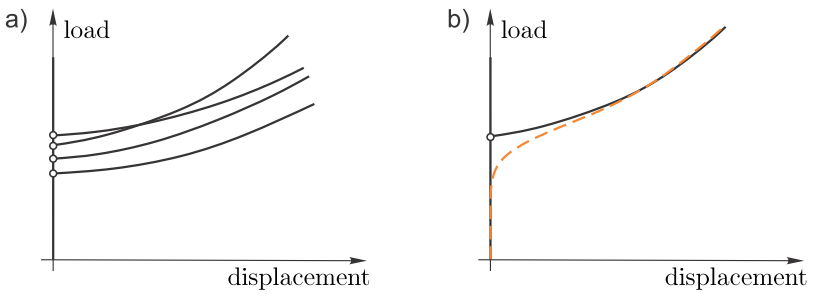

Fig. 6. Conceptualization of: (a) a cluster of stable bifurcation points for a symmetrical structure; (b) a primary and secondary equilibrium paths at first stable bifurcation point for a symmetrical structure without (solid black line) and with asymmetric imperfections (dashed red line).

At the transition to the secondary path, the dimples were beginning to form; the critical pressure for this particular example was $p \approx -238$ kPa. With further increase in pressure, the depth of dimples increased and their arrangement remained the same within the observed pressure interval.

We stopped the analysis at $p \approx -265$ kPa. At this point, we calculated the characteristic wavelength λ on fully developed dimple pattern, using the Delaunay triangulation on the dimple centres, and found that $\lambda = 6.868 \pm 0.379$ mm. For comparison, an analytical formula (see Eq. (1) in Ref. [32]) gives $\lambda = 7.283$ mm; a relative difference of approximately 5.7 %. The number of dimples we counted in this simulation was 124.

In addition to the sphere presented in Fig. 5, we performed simulations on three other spherical examples with the same mesh of 148,512 elements. In Fig. 7 we present their fully developed patterns. For thicknesses and moduli of elastic foundations given in the caption of Fig. 7, we obtain dimple patterns with characteristic wavelengths $\lambda = (3.471, 5.165, 6.868, 8.667)$ mm and standard deviations (0.270, 0.323, 0.379, 0.481) mm, respectively. As expected, a thinner shell with stiffer foundation exhibits a pattern with a shorter wavelength. The theoretical prediction, using the formula from Eq. (1) in Ref. [32], yields $\lambda = (3.642, 5.463, 7.283, 9.104)$ mm, which represents a (4.7, 5.4, 5.7, 4.8) % relative

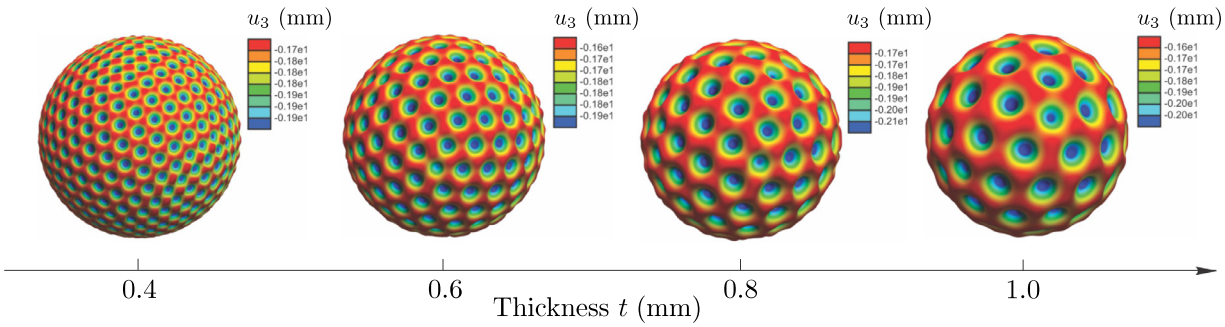

Fig. 7. Fully developed wrinkling patterns on spheres with different thicknesses, $t = (0.4, 0.6, 0.8, 1.0)$ mm, moduli of elastic foundation, $K_s = (0.2610, 0.1738, 0.1302, 0.1039)$ N/mm^3, pressure loads $p = -(492.0, 323.5, 261.8, 214.7)$ kPa, and all with the same shell radius $R = 20.0$ mm, Young's modulus $E = 2.1$ MPa and Poisson ratio $\nu = 0.49$. The number of dimples is $N = (490, 220, 124, 78)$ and the number of elements in the mesh is $n = 148\,512$ for all four examples.

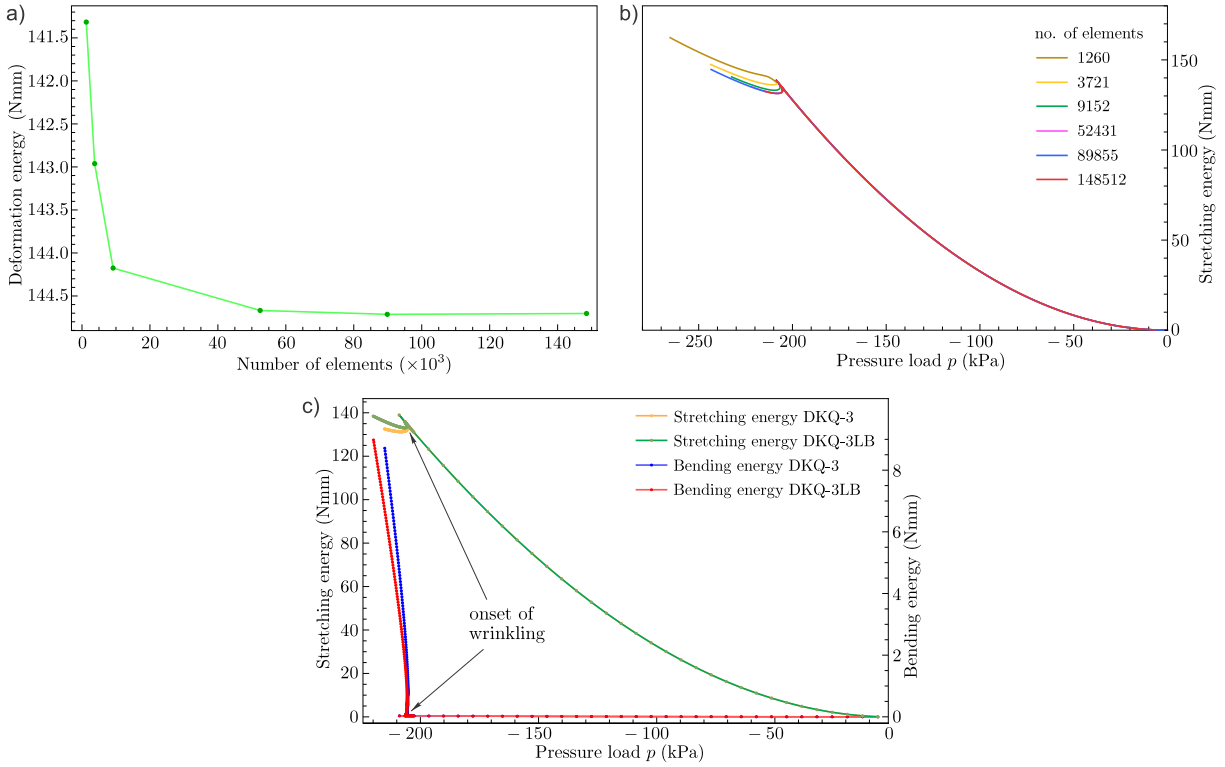

Fig. 8. Convergence and comparison diagrams for a spherical shell with $t = 1$ mm (material and geometric properties are the same as above). (a) Convergence of the shell's deformation energy (sum of stretching and bending energy) as the number of elements (mesh density) is increased. All values of deformation energy are obtained at pressure load $p = 215$ kPa. (b) Six plots of the stretching energy versus pressure, showing the convergence as the number of elements is increased. (c) Stretching and bending energies obtained via finite element analysis with a fully nonlinear element (DKQ-3) and nonlinear-stretching-linear-bending element (DKQ-3LB). Dark yellow and blue color correspond to the nonlinear solution, whereas green and red correspond to the solution with linear bending. The number of elements in the mesh was $n = 148\,512$. (For interpretation of the references to colour in this figure legend, the reader is referred to the web version of this article.)

difference as compared to the wavelength obtained from our numerical simulations. We note that in general simulations become more difficult to perform with decreasing wavelength, because the number of meta-stable states grows rapidly (see Refs. [32,33] for more details). In our simulations, however further possible critical points along the secondary equilibrium path were not studied.

To check the convergence of our numerical procedure, we carried out six simulations on each sample using increasingly refined meshes, with 1260, 3721, 9152, 52,431, 89,855 and 148,512 finite elements. Fig. 8a shows the convergence of the deformation energy at $p = 215$ kPa as the mesh for the shell with thickness $t = 1$ mm from Fig. 7 is refined. The convergence diagram shows that a fine mesh (i.e more than 50,000 elements) is needed for a sufficiently accurate result. Similar convergence diagrams were obtained for all four shell configurations from Fig. 7.

Another convergence diagram, which shows the stretching energy as a function of the pressure for all six tested mesh densities, is given in Fig. 8b. The results overlap in the sub-critical region, whereas the difference becomes evident only after the loss of stability of the shell. Analogous to Fig. 8a, the system responds as more compliant for coarser meshes, and exhibits practically identical response for the finest two meshes in the post-critical region as well.

In Fig. 8c, we plot the stretching (i.e., the membrane) and bending parts of the shell's deformation energy as a function of pressure. It can be noticed, that the stretching energy increases in the initial stage of the simulation as the displacement field is changing due to the (almost) homogeneous compression (i.e., the surface remains almost spherical). Simultaneously, the bending energy is still approximately equal to zero until the shell looses its stability around the critical pressure. At this pressure, it is energetically more favourable for the shell to locally bend than to (almost homogeneously) compress further. This can be seen from the diagrams on Fig. 8c; the shell starts to wrinkle when a small unloading (i.e., relaxation) occurs in the stretching energy (finer the mesh is, the larger unloading) along with a rapid increase in bending energy. For the comparison of energies, we used two versions of the finite element derived above, which we denote as DKQ-3 and DKQ-3LB. The original DKQ-3 element (which we used for computations in all examples) keeps all the nonlinear terms of our reduced model, and the DKQ-3LB element comprises nonlinear stretching and linear bending terms from Eq. (36) (the latter has the same structure as the one used in study [22]). Curves plotted in Fig. 8c in dark yellow and green color represent the stretching energy whereas the blue and red represent the bending energy. The difference between the results obtained with DKQ-3 and DKQ-3LB elements is distinguishable only after the loss of stability, as expected. These results diverge as the system is pushed further into the post-buckling regime with increasing pressure.

4.3. Hemispherical shell

The material and geometric properties for the hemispherical shell presented in Fig. 9 are the same as given in the caption of Fig. 5 for the full sphere. The shell boundary around the equator was free, since no displacement or rotation degrees of freedom were restrained on the elements.

Numerical simulation was performed in a similar manner as for the previous examples. We present its results in Fig. 9, by showing a pressure-displacement diagram and a set of patterns calculated at different pressure levels to show the pattern evolution. The node which was traced in the path-following algorithm was located at the center of the dimple closest to the apex of the hemisphere.

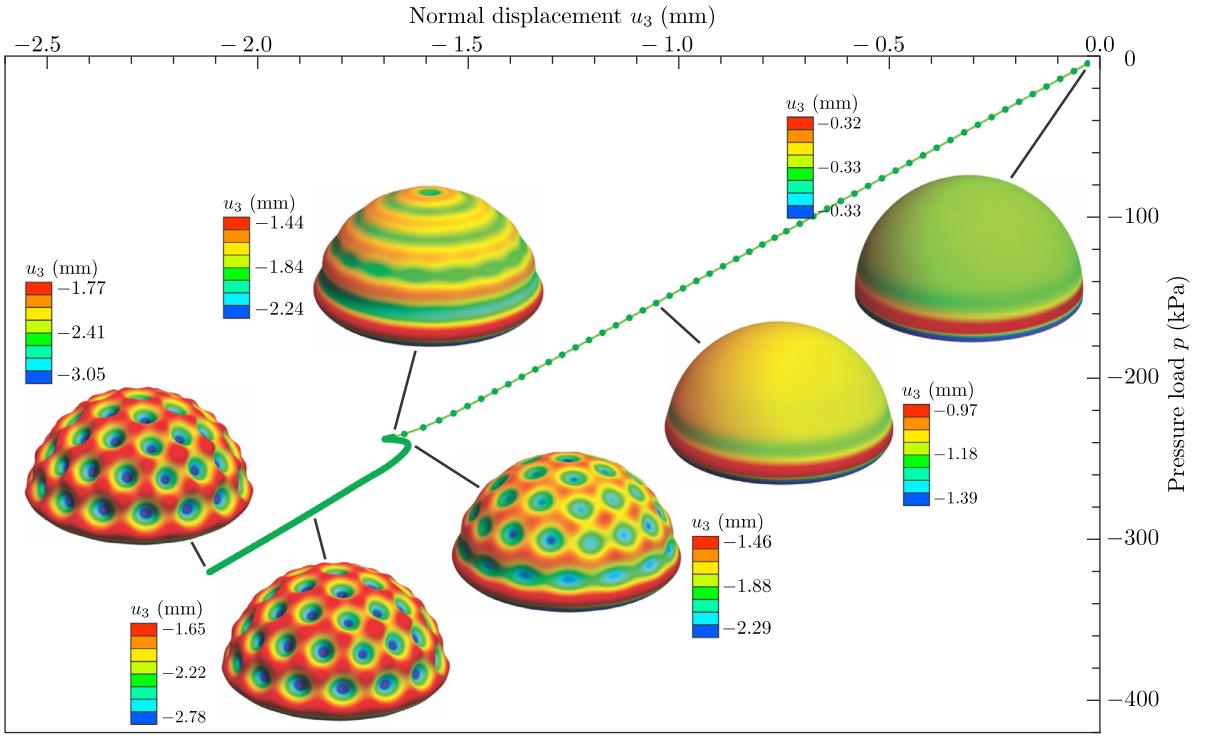

Fig. 9. Development of the normal displacement field u_3 on a hemispherical shell as the pressure p is increased. Geometrical and material parameters are the same as in the caption of Fig. 5. The number of elements in the mesh was $n = 94\,212$.

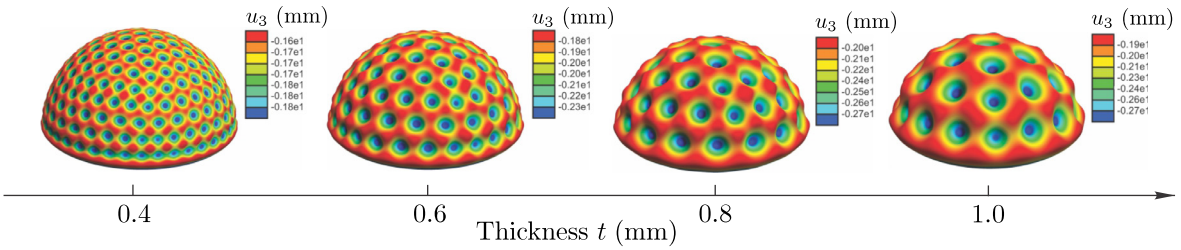

Fig. 10. Fully developed wrinkling patterns on hemispheres with different thicknesses, $t = (0.4, 0.6, 0.8, 1.0)$ mm, moduli of elastic foundation, $K_s = (0.2610, 0.1738, 0.1302, 0.1039)$ N/mm^3, pressure loads $p = -(469.7, 369.2, 287.2, 256.4)$ kPa, and all with the same shell radius $R = 20.0$ mm, Young's modulus $E = 2.1$ MPa, and Poisson ratio $\nu = 0.49$. The number of dimples is $N = (268, 122, 67, 47)$ and the number of elements in the mesh is $n = 94\,212$ for all four examples..

It can be noticed that the sub-critical response of the shell is (slightly) nonlinear, as opposed to the full spherical shell on Fig. 5. This is because the initial deformation is not homogeneous due to the open boundary effect. Namely, the first deformation mode which we observe around the equator at lower pressure values, resembles a formation of an elephant's foot (which is otherwise characteristic for an elasto-plastic buckling of thicker axisymmetrical shells, see e.g. [38,50]). Still in the sub-critical regime, slightly below the critical pressure, this mode starts to propagate towards the apex, forming an axisymmetric deformation mode over the complete shell with concentric circular valleys. With further increase in the pressure, these valleys evolve into dimples (and slightly rearrange) around the critical pressure $p \approx -238$ kPa. It is interesting to note that we find a snap-back in the pressure-displacement curve at the critical pressure, unlike in the case of a full sphere. The mechanism of passing the first bifurcation point on the way to the secondary equilibrium path is still the same as mentioned above.

In addition to the hemisphere presented in Fig. 9, we analyzed three other hemispherical shells with different geometric and material properties. We used the same values of material and geometric parameters as in the cases of full spheres (see the caption of Fig. 7), and obtained similar results, as expected. Their fully developed wrinkling patterns are presented in Fig. 10. The only major difference in comparison to the wrinkling patterns of full spheres was found at the edges of hemispheres, where the arrangement of dimples is concentric with the equator (which affects the distribution of dimples) and the stiffness of the shell is smaller (which affects the size of the dimples). Thus, we considered only dimples away from the edge to calculate the characteristic wavelength. We calculated the following characteristic wavelengths: $\lambda = (3.488, 5.149, 6.988, 8.552)$ mm with standard deviation (0.317, 0.425, 0.528, 0.817) mm, for thicknesses $t = (0.4, 0.6, 0.8, 1.0)$ mm, respectively. As the theoretical prediction is the same as before (because we considered the same geometric and material properties), we got a (4.2, 5.7, 4.1, 6.1) % relative difference as compared to the wavelength obtained from our numerical analysis.

4.4. Spheroidal shell

We analyzed three different spheroidal shells with the principal axis ratios of $b/a = (0.7, 1.1, 2.0)$ and $c/a = 1$. One axis was held fixed at $a = 20$ mm. Each shell was simulated four times, every time using a different thickness, $t = (0.4, 0.6, 0.8, 1.0)$ mm. The modulus of elastic foundation K_s was calculated, as before, from Eq. (B.10) in Ref. [27], for each configuration.

The results of our simulations shown in Fig. 11 illustrate the wrinkling pattern dependance on the shell thickness, substrate rigidity and (variable) curvature of the system. With respect to varying thickness and substrate rigidity, simulations yield qualitatively the same results as in the cases of spheres and hemispheres, in which larger shell thickness and lower substrate rigidity result in patterns with longer wavelengths. For the principal axes ratio $b/a = 0.7$, shown in the bottom row of Fig. 11, we find dimples across the whole surface in each sample – similar to what we found on spheres. As demonstrated in the first row of Fig. 12, they are formed first at the poles since the flexural rigidity is the smallest there, and then spread with increasing pressure towards the equator until the surface is fully covered.

In contrast, different modes are obtained across each surface for $b/a = 1.1$ and $b/a = 2.0$ in Fig. 11, as expected from the non-constant Gaussian curvature of the spheroid. The first example in the middle row exhibits a mode mixed of dimples and creases. The creases are formed around the equator of the spheroid from small dents which appear there first (in the region with the smallest rigidity) and grow with increase in pressure into grooves oriented perpendicular to the equator, as shown in the second row of Fig. 12. In this particular case, the spheroidal caps (regions around the poles) are covered by dimples later in the simulation. The remaining three shells in the middle row show smooth and unbuckled caps since the flexural rigidity of the shell (due to curvature, thickness and substrate rigidity) is there large enough to suppress the local snapping of the shell at that pressure load. We assume that dimples would appear on these caps as well if the simulation would converge further.

Note that similar observations on spheroids were reported in studies by Yin et al. [30,31] using Abaqus and simplified analytical models.

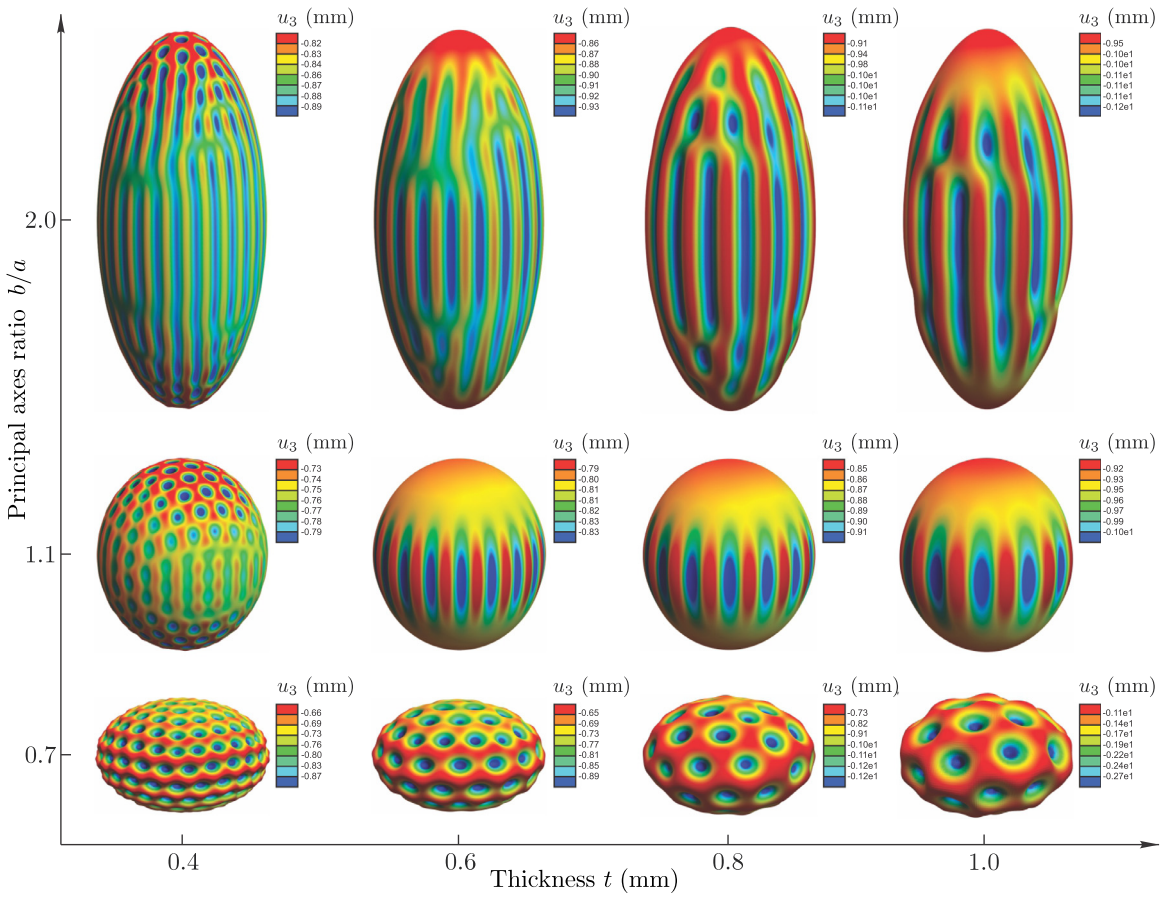

Fig. 11. Wrinkling on spheroids with principal axes ratios $b/a = (0.7, 1.1, 2.0)$ and thicknesses $t = (0.4, 0.6, 0.8, 1.0)$ mm. The modulus of elastic foundation is the same for all three shells in each column, $K_s = (0.0534, 0.0355, 0.0265, 0.0211)$ N/mm^3.

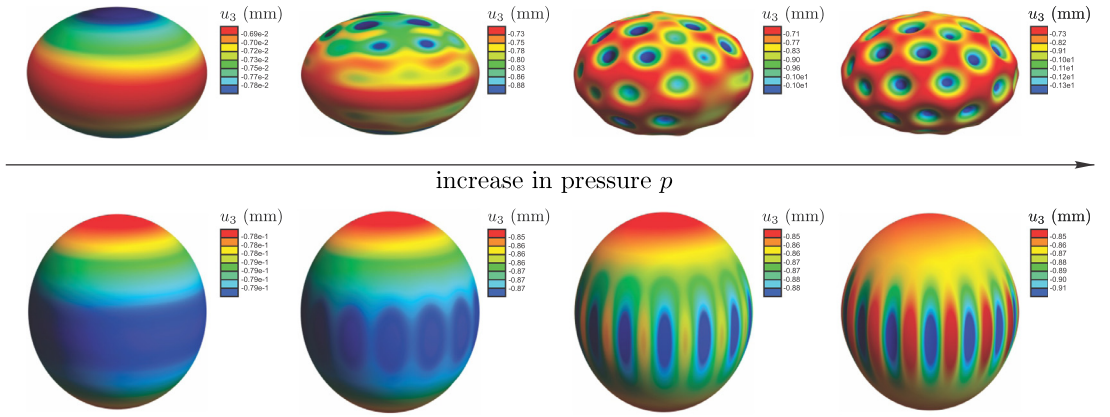

Fig. 12. Development of the pattern on two spheroids as the pressure p is increased. Upper row: principal axes ratio $b/a = 0.7$, thickness $t = 0.8$ mm, $K_s = 0.0265$ N/mm^3. Lower row: principal axes ratio $b/a = 1.1$, thickness $t = 0.8$ mm, $K_s = 0.0265$ N/mm^3. The snap-shots of both spheroids are not taken at the same pressure levels.

5. Conclusion

We derived a finite element formulation for quantitative prediction of surface wrinkling of pressurized elastic shells attached to compliant substrates. Our theory is build on three basic assumptions which involve the Kirchhoff-Love shell kinematics, the approximation of the substrate response by a Winkler foundation and a model order reduction of the displacement field by neglecting the tangential displacements.

Two types of finite elements were formulated. The DKQ-3 element which keeps all the nonlinear terms of our reduced model and the DKQ-3LB element which comprises nonlinear stretching and linear bending terms. A comparison between both types of elements shows that the difference is evident in the post-buckling regime, where the results diverge with increasing pressure. It should also be mentioned that an advanced path-following method [39] was employed in our computations and that our numerical approach did not require any perturbations (either in the initial geometry or in the load) to incite the transition from the fundamental equilibrium path to the secondary one for double curved shells, due to the inherent asymmetric imperfections in the mesh.

Numerical simulations using the DKQ-3 element on full spheres, hemispheres and spheroids show a very good quantitative agreement with theoretical predictions and experiments on wavelength as well as the qualitative depiction of the pattern evolution (see e.g. [30,32]). Nevertheless, we obtain characteristically higher pressure values in our calculations as compared to experiments from Ref. [32]. We attribute this difference to the blind use of the foundation stiffness formula (which otherwise contains the material parameters of both, the shell and the solid elastic foundation) which is originally developed for cylinders and as such, not tailored for our specific problems. Moreover, it is evident from the available literature that the exact expression for the spring stiffness of the Winkler type foundation still remains an open problem for general shapes of shells. Alternatively, the DKQ-3 finite element could be used in combination with a 3D solid finite element (also with appropriate kinematic reduction and incompatible modes to account for near incompressibility of the substrate) to obtain a good match also for pressure. But the obvious drawback of this idea lies in the fact that several layers of solid elements would have to be included across the thickness of the substrate, which would increase the computational time considerably.

Overall, we can conclude that the proposed computational model provides a sound basis for a robust nonlinear finite element formulation that is worth developing further in order to study wrinkling of thin shells attached to elastic substrates.

Acknowledgments

The authors thank Dr. Andjelka Stanić for helpful suggestions regarding finite element implementation and solution procedures. M.B. acknowledges the financial support from the Slovenian Research Agency (research core funding No. J2-9223).

References

[1] Wieghardt K. Über den balken auf nachgiebiger unterlage. Z angew Math Mech 1922;2(3):165–84.
[2] Biot MA. Bending of an infinite beam on an elastic foundation. J Appl Mech 1937;4:1–7.
[3] Reissner ME. On the theory of beams resting on a yielding foundation. Proc Natl Acad Sci USA 1937;23(6):328–33.
[4] Gough GS, Elam CF, Tipper GH, De Bruyne NA. The stabilisation of a thin sheet by a continuous supporting medium. Aeronaut J 1940;44(349):12–43.
[5] Allen HG. Analysis and design of structural sandwich panels. New York: Pergamon Press; 1969.
[6] Stafford CM, Harrison C, Beers KL, Karim A, Amis EJ, VanLandingham MR, Kim HC, Volksen W, Miller RD, Simonyi EE. A buckling-based metrology for measuring the elastic moduli of polymeric thin films. Nat Mater 2004;3:545–50.
[7] Chandra D, Yang S. Strain responsive concave and convex microlens arrays. Appl Phys Lett 2007;91:251912(3).
[8] Chan EP, Crosby AJ. Fabricating microlens arrays by surface wrinkling. Adv Mater 2006;18(24):3238–42.
[9] Chan EP, Smith EJ, Hayward RC, Crosby AJ. Surface wrinkles for smart adhesion. Adv Mater 2008;20(4):711–16.
[10] Yang S, Krishnacharya K, Lin PC. Harnessing surface wrinkle patterns in soft matter. Adv Funct Mater 2010;20(16):2550–64.
[11] David CS, Crosby AJ. Mechanics of wrinkled surface adhesion. Soft Matter 2011;7(11):5373–81.
[12] Chung JY, Youngblood JP, Stafford CM. Anisotropic wetting on tunable micro-wrinkled surfaces. Soft Matter 2007;3(9):1163–9.
[13] Terwagne D, Brojan M, Reis PM. Smart morphable surfaces for aerodynamic drag control. Adv Mater 2014;26(38):6608–11.
[14] Huang Z, Hong W, Suo Z. Nonlinear analyses of wrinkles in a film bonded to a compliant substrate. J Mech Phys Solids 2005;53(9):2101–18.
[15] Audoly B, Boudaoud A. Buckling of a stiff film bound to a compliant substrate-part i: formulation, linear stability of cylindrical patterns, secondary bifurcations. J Mech Phys Solids 2008;56(7):2401–21.
[16] Cai S, Breid D, Crosby AJ, Suo Z, Hutchinson JW. Periodic patterns and energy states of buckled films on compliant substrates. J Mech Phys Solids 2011;59(5):1094–114.
[17] Cao G, Chen X, Li C, Ji A, Cao Z. Self-assembled triangular and labyrinth buckling patterns of thin films on spherical substrates. Phys Rev Lett 2008;100(3):036102(4).
[18] Abaqus, Dassault Systemes, Abaqus, http://www.3ds.com/productsservices/simulia/products/abaqus/.
[19] Breid D, Crosby AJ. Curvature-controlled wrinkle morphologies. Soft Matter 2013;9(13):3624–30.
[20] Yin J, Han X, Cao Y, Lu C. Surface wrinkling on polydimethylsiloxane microspheres via wet surface chemical oxidation. Sci Rep UK 2014;4:5710(8).
[21] Li B, Fei J, Cao JP, Feng XQ, Gao H. Surface wrinkling patterns on a core-shell soft sphere. Phys Rev Lett 2011;106(23):234301(4).
[22] Stoop N, Lagrange R, Terwagne D, Reis PM, Dunkel J. Curvature-induced symmetry breaking determines elastic surface patterns. Nat Mater 2015;14:337–42.
[23] Ciarlet PG. Mathematical elasticity, 3; 2000. North Holland, Amsterdam
[24] Xu F, Potier-Ferry M. On axisymmetric/diamond-like mode transitions in axially compressed core-shell cylinders. J Mech Phys Solids 2016;94:68–87.
[25] Damil N, Potier-Ferry M. A new method to compute perturbed bifurcations: application to the buckling of imperfect elastic structures. Int J Eng Sci 1990;28(9):943–57.
[26] Zhano Y, Cao Y, Feng XQ, Ma K. Axial compression-induced wrinkles on a core-shell soft cylinder: theoretical analysis, simulations and experiments. J Mech Phys Solids 2014;73:212–27.
[27] Lagrange R, Jimenez FL, Terwagne D, Brojan M, Reis PM. From wrinkling to global buckling of a ring on a curved substrate. J Mech Phys Solids 2016;89:77–95.
[28] Bohinc U, Brank B, Ibrahimbegovic A. Discretization error for the discrete kirchoff plate finite element approximation. Comput Method Appl M 2014;269:415–36.
[29] Bohinc U, Ibrahimbegovic A, Brank B. Model adaptivity for finite element analysis of thin or thick plates based on equilibrated boundary stress resultants. Eng Comput (Swansea) 2009;26(1/2):69–99.
[30] Yin J, Cao Z, Li C, Sheinman I, Chen X. Stress-driven buckling patterns in spheroidal core/shell structures. P Natl Acad Sci USA 2008;105(49):19132–5.
[31] Yin J, Chen X, I Sheinman I. Anisotropic buckling patterns in spheroidal film/substrate systems and their implications in some natural and biological systems. J Mech Phys Solids 2009;57:1470–84.

[32] Brojan M, Terwagne D, Lagrange R, Reis PM. Wrinkling crystallography on spherical surfaces. P Natl Acad Sci USA 2015;112(1):14–19.
[33] Erber T, Hockney GM. Equilibrium configurations of n equal charges on a sphere. J Phys A Math Gen 1991;24(23):1369–77.
[34] Betsch P, Gruttmann F, Stein E. A 4-node finite shell element for the implementation of general hyperelastic 3D-elasticity at finite strains. Comput Meth Appl Mech Eng 1996;130:57–79.
[35] Brank B, Korelc J, Ibrahimbegović A. Nonlinear shell problem formulation accounting for through-the-thickness stretching and its finite element implementation. Comp Struct 2002;80:699–717.
[36] Brank B. Nonlinear shell models with seven kinematic parameters. Comput Meth Appl Mech Eng 2005;194:2336–62.
[37] Simo JC, Fox DD. On a stress resultant geometrically exact shell model. part i: formulation and optimal parametrization. Comput Meth Appl Mech Eng 1989;72:267–304.
[38] Brank B, Peri D, Damjanić FB. On large deformations of thin Elasto-plastic shells: implementation of a finite rotation model for quadrilateral shell element. Int J Numer Methods Eng 1997;40:689–726.
[39] Stanić A, Brank B, Korelc J. On path-following methods for structural failure problems. Comput Mech 2016;58:281–306.
[40] Naghdi PM. The theory of shell and plates, mechanics of solids, vol II, linear theories of elasticity and thermoelasticity. In: Truesdell C, editor. Linear and nonlinear theories of rods, plates and shells. Berlin, Heidelberg: Springer-Verlag; 1973. p. 426–640.
[41] Xu F, Potier-Ferry M. Quantitative predictions of diverse wrinkling patterns in film/substrate systems. Sci Rep 2017;7:18081.
[42] Jia F, Li B, Feng XQ. Wrinkling pattern evolution of cylindrical biological tissues with differential Growts. Phys Rev 2015;E91:012403.
[43] Wu J, Chen X. Buckling patterns of conical thin film/substrate systems. J Phys D Appl Phys 2013;46:155306.
[44] Simo JC, Hughes TJR. On the variational foundations of assumed strain methods. J Appl Mech 1986;53(1):51–4.
[45] Korelc J, Wriggers P. Automation of finite element methods. Springer Inter-national Publishing; 2016.
[46] Wolfram Research, Inc. Mathematica, Version 11.3. IL: Champaign; 2018.
[47] Brank B, Damjanić FB, Peri D. On implementation of a nonlinear four node shell finite element for thin multilayered elastic shells. Comput Mech 1995;16(5):341–59.
[48] Riks E. Buckling analysis of elastic structures: a computational approach. Adv Appl Mech 1997;24:1–76.
[49] Kegl M, Brank B, Harl B, Oblak MM. Efficient handling of stability problems in shell optimization by asymmetric worst-case shape imperfection. Int J Numer Meth Eng 2008;73:1197–216.
[50] Dujc J, Brank B. Stress resultant plasticity for shells revisited. Comput Meth Appl Mech Eng 2012;247/248:146–65.